Am J Cancer Res 2026;16(3):1042-1055
www.ajcr.us /ISSN:2156-6976/ajcr0170964

Original Article

Predictive value of computed tomography radiomics for lymphatic-vascular space infiltration in colon cancer

Jiexia Lv[1], Huajun Yu[2]

[1]*Department of Radiology, Yongkang First People's Hospital, Yongkang 321300, Zhejiang, China;* [2]*Department of Radiology, Zhejiang Hospital, Hangzhou 310013, Zhejiang, China*

Received December 22, 2025; Accepted March 19, 2026; Epub March 25, 2026; Published March 30, 2026

Abstract: This study aimed to construct and validate a preoperative predictive model for lymphatic-vascular space infiltration (LVSI) in colon cancer using clinical features and computed tomography (CT) radiomics, and to evaluate its clinical utility. A total of 244 colon cancer patients treated at Yongkang First People's Hospital from January 2018 to January 2024 were enrolled as the training set (LVSI-positive: n=92, LVSI-negative: n=152), and 58 patients treated between February 2024 and August 2025 served as the validation set. Clinical data were collected, and contrast-enhanced CT images were analyzed. Radiomic features were extracted using PyRadiomics, and features with intraclass correlation coefficient (ICC) >0.8 were retained to ensure reproducibility, and least absolute shrinkage and selection operator (LASSO) regression was applied for dimensionality reduction. A clinical model, a radiomics model (based on Rad-score), and a combined model were established via multivariate logistic regression. Receiver operating characteristic (ROC) curve, calibration curve, Hosmer-Lemeshow test, and decision curve analysis (DCA) were used to assess model performance. The results showed that tumor diameter, differentiation degree, CT-detected extramural vascular invasion (cEMVI), and carcinoembryonic antigen (CEA) were independent risk factors for LVSI (all P<0.05). Four key radiomic features were screened to calculate Rad-score. In the training set, the combined model achieved an area under the curve (AUC) of 0.90 (95% CI: 0.86-0.94), significantly higher than the clinical model (AUC=0.75) and radiomics model (AUC=0.84) (both P<0.001), with accuracy, sensitivity, and specificity of 0.82, 0.80, and 0.86, respectively. In the validation set, the combined model maintained an AUC of 0.92 (95% CI: 0.86-0.99), outperforming the clinical model (AUC=0.71, P=0.004), and showed good calibration (Hosmer-Lemeshow P=0.364) and positive net benefits in DCA. The combined model integrating clinical features and CT radiomics exhibits excellent performance in preoperative prediction of LVSI in colon cancer, providing a reliable tool for individualized treatment decision-making.

Keywords: Colon cancer, computed tomography radiomics, lymphatic-vascular space infiltration, predictive value

Introduction

Colon cancer is a common malignant tumor of the digestive system with high incidence and mortality rates worldwide [1]. According to epidemiological estimates, the disease burden of colon cancer is particularly severe in China [2]. The incidence of colon cancer is projected to further increase by 2030 [3]. Despite significant advances in medical technology in recent years, the overall prognosis for colorectal cancer patients remains suboptimal [4]. Lymphatic-vascular space infiltration (LVSI) refers to the presence of tumor cells within the spaces between lymphatic vessels or blood vessel walls [5]. The presence of LVSI is not only closely associated with patient prognosis but also significantly influences treatment decision-making, particularly the selection of adjuvant chemotherapy and the determination of surgical extent [6]. Specifically, LVSI positivity is a key factor in determining whether to administer adjuvant chemotherapy in stage II colon cancer and may influence the extent of lymphadenectomy during surgery, as it indicates a higher risk of occult metastasis [7, 8]. However, the diagnosis of LVSI still relies on postoperative pathological examination and therefore cannot provide timely information for individualized treatment planning before surgery [8]. Therefore, the development of a non-invasive, reproducible and readily applicable preoperative predictive tool has become an urgent need for optimizing colorectal cancer treatment strategies

https://doi.org/10.62347/AFQS4886

and mitigating the risks of overtreatment or undertreatment.

Currently, contrast-enhanced computed tomography (CT) remains the primary tool for preoperative assessment in clinical practice, enabling preliminary assessment of disease status through observation of tumor size, lymph node morphology, and distant metastasis [9]. However, the direct predictive value of CT for LVSI remains limited, and its sensitivity and specificity need to be improved [10]. In addition, although serum tumor markers such as carcinoembryonic antigen (CEA) and carbohydrate antigen 19-9 (CA19-9) can assist in evaluating tumor activity, their specificity is limited and they cannot effectively determine LVSI status when used alone [11]. As an emerging quantitative imaging technology, radiomics enables the extraction and analysis of high-throughput features from medical images, thereby uncovering tumor heterogeneity imperceptible to the naked eye [12]. By constructing predictive models based on these features, radiomics offers a promising avenue for non-invasive assessment of tumor biological behavior. Its predictive value for tumor characteristics and prognosis has been validated in several malignancies such as lung and breast cancer [13, 14]. In the context of colorectal cancer, preliminary radiomics studies have primarily focused on predicting outcomes like lymph node metastasis, tumor staging, or treatment response [15, 16]. However, studies specifically targeting the preoperative prediction of LVSI remains limited. Furthermore, most existing studies suffer from key methodological limitations, such as small single-center sample sizes and the absence of external validation, which raises concerns about model overfitting and generalizability [17].

Against this backdrop, the present study aimed to construct and validate a predictive model for LVSI in colon cancer based on CT radiomics. By collecting data from colon cancer patients who underwent contrast-enhanced CT examinations and using postoperative pathological findings as the gold standard, we extracted and screened radiomic features closely associated with LVSI. Subsequently, a clinical model, a CT radiomics model, and a combined model were established. The diagnostic performance of these models were further evaluated using receiver operating characteristic (ROC) curve analysis, and their clinical utility was further assessed using decision curve analysis (DCA). We anticipate that these findings will provide valuable evidence for preoperative risk stratification and treatment decision-making in colon cancer patients, thereby improving patient prognosis and quality of life.

Materials and methods

Study population

This study retrospectively retrieved patient data from the electronic medical system. A total of 244 patients with colon cancer who were treated at Yongkang First People's Hospital from January 2018 to January 2024 were retrieved. The study flowchart is shown in **Figure 1**. After applying strict inclusion and exclusion criteria, data of 244 patients were finally collected for statistical analysis and constituted the training cohort.

For the training set, considering that the study aimed to identify independent risk factors for LVSI (a dichotomous outcome) and construct a multivariate logistic regression model, the sample size was determined according to the "10 events per variable (EPV)" rule [18]. Preliminary clinical data showed that the LVSI positive rate in colon cancer patients was approximately 38% (consistent with the final training set positive rate of 37.7%, 92/244). In the initial model design, 4 potential clinical variables (tumor diameter, differentiation degree, cEMVI, CEA) and 4 core radiomic features, totaling 8 variables, were planned to be included. Thus, the minimum required number of LVSI-positive cases (events) was 8 × 10 = 80. Based on previous similar retrospective radiomics studies on colon cancer [16], the expected data loss rate due to incomplete medical records or unqualified imaging data was estimated to be approximately 15-20%. To compensate for potential data loss or exclusion (consistent with the reported loss rate in similar studies), the sample size was increased by 20%, leading to a target of 96 LVSI positive cases. Finally, 244 patients (including 92 LVSI positive cases) were enrolled in the training set, which satisfied the EPV requirement (92 events/8 variables = 11.5 EPV). In addition, to validate the predictive model, an independent validation cohort comprising 58 patients treated between February 2024 to August 2025 was collected. The inclusion and exclusion criteria for the validation set

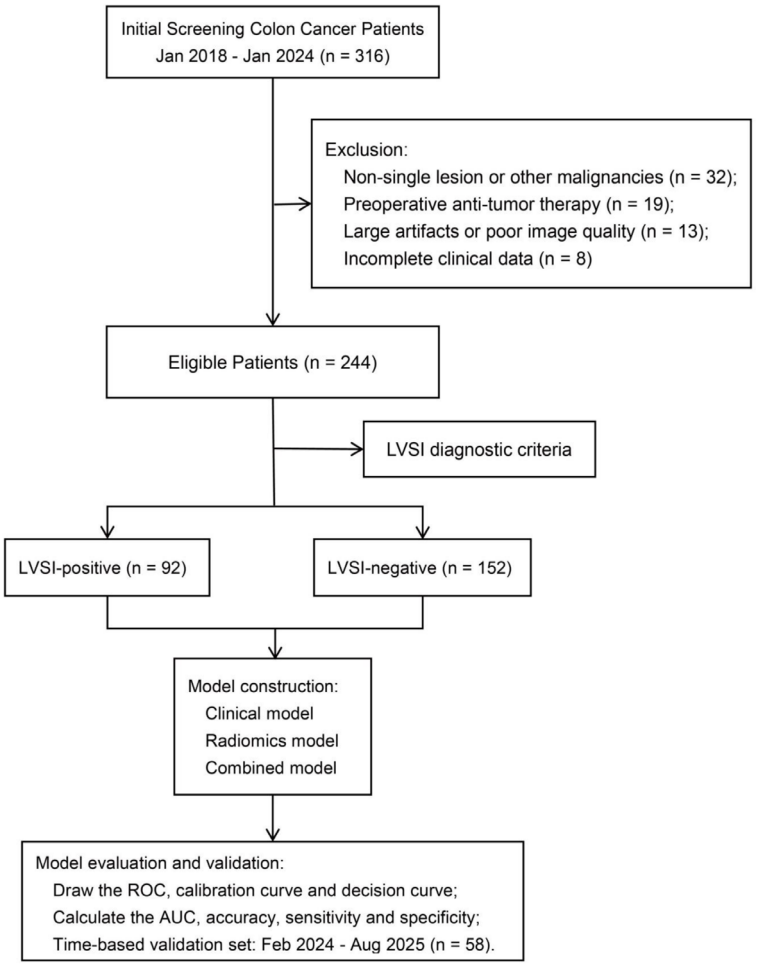

Figure 1. Flow chart of the study design and patient selection.

were exactly the same as those in the training set. This study strictly adhered to the principles of the Declaration of Helsinki and was approved by the Ethics Committee of Yongkang First People's Hospital (Approval Number: EC2025-LW-028-01(K)).

LVSI diagnostic criteria

The pathological diagnosis of LVSI was established in accordance with the criteria recommended by the World Health Organization (WHO) Classification of Tumors: Digestive System Tumors [19] and independently completed by two senior pathologists with over 10 years of experience in gastrointestinal pathology. The diagnostic criteria were defined as follows: Tumor cells (single cells, clusters, or nests) were identified within the endothelial-lined lymphatic or vascular spaces, with clear separation from the surrounding stroma by endothelial cells. Hematoxylin-eosin (HE) staining was initially used for screening: pathologists observed the presence of tumor cells in lymphatic/vascular lumens, combined with morphological features such as vascular wall structure and surrounding tissue infiltration. If HE staining results were ambiguous (e.g., unclear endothelial lining or questionable tumor cell localization), immunohistochemical staining was additionally performed using the lymphatic endothelial marker D2-40 and the vascular endothelial marker CD34 to clarify the nature of the vascular structures and confirm the presence of tumor cell infiltration. Discrepancies between the two pathologists were resolved through joint review and consensus after re-examination of the slides.

Inclusion and exclusion criteria

Inclusion criteria: (1) age ≥18 years old; (2) patients diagnosed with colon cancer based on postoperative pathological examination, presenting with a single lesion; (3) A contrast-enhanced CT scan was conducted four weeks before the operation, with clear results, and no radiotherapy, chemotherapy, or other anti-tumor interventions that may alter tumor morphology were performed during the interval between CT examination and surgery; (4) patients who had not received any anti-tumor treatment before surgery.

Exclusion criteria: (1) patients with other malignant tumors; (2) patients with incomplete clinical or pathological records; (3) CT images with severe artifacts that prevented accurate delineation of the region of interest (ROI).

Clinical data and image acquisition

Baseline clinical data were collected for each patient from the electronic medical records system, including: sex, age, body mass index

(BMI), primary tumor location, preoperative CEA and CA19-9 levels, biopsy-based tumor differentiation, CT-based extramural venous invasion (cEMVI), pericolonic/perirectal fat infiltration (assessed on CT as the loss of the fat plane between the tumor and adjacent structures, with stranding or nodular soft-tissue density extending into the surrounding pericolonic/perirectal fat), and the maximum tumor diameter (mm) measured on CT images. All patients had no radiotherapy, chemotherapy, or other interventions affecting tumor morphology between CT scanning and surgery, ensuring consistency between imaging tumor status and intraoperative findings.

All patients underwent contrast-enhanced CT examinations using either a Siemens Somatom Definition 64-slice CT scanner (Siemens Medical Systems AG, Erlangen, Germany) or a GE LightSpeed 16-row CT scanner (General Electric Healthcare, Milwaukee, USA). The scanning parameters were as follows: tube voltage, 120 kV; tube current, 120 mA; slice thickness, 5 mm; slice spacing, 5 mm. All patients underwent plain and contrast-enhanced scans (arterial phase, venous phase, and delayed phase). A non-ionic iodinated contrast agent (iodine concentration: 320 mgI/mL) was administered via the antecubital vein using a high-pressure injector at a flow rate of 3.0 mL/s, with a dose of 1.0 mL/kg body weight. The arterial, venous, and delayed phase scans were obtained at 30 s, 70 s, and 180 s after contrast injection, respectively. The reconstructed images were transferred to the Picture Archiving and Communication System (PACS) workstation for subsequent analysis.

Radiomics process

(1) Image segmentation: all CT images were exported in Digital Imaging and Communications in Medicine (DICOM) format and imported into the Picture Archiving and Communication System (PACS) for image analysis. Two radiologists with over ten years' experience in abdominal imaging diagnosis independently delineated the entire tumor margin by manually contouring all consecutive cross-sectional images to generate regions of interest (ROIs), while being blinded to the pathological findings. Discrepancies were resolved through mutual consultation. All planar ROIs were superimposed to generate a three-dimensional volume of interest (VOI) for subsequent radiomic feature extraction.

(2) Feature extraction: radiomics features were extracted from each VOI using the open-source Python package PyRadiomics (version 3.0.1). A total of 1,535 quantitative features were extracted, including first-order statistical features, shape features, greyscale co-occurrence matrix (GLCM) features, greyscale run length matrix (GLRLM) features, greyscale size-zone matrix (GLSZM) features, neighborhood greyscale difference matrix (NGTDM) features, and filtered image features based on Laplacian-Gaussian (LoG) filtering and wavelet transformation. To minimize the impact of variations in CT scanners and acquisition parameters on feature reproducibility, all images were resampled to an isotropic voxel spacing of 1 × 1 × 1 mm^3 using B-spline interpolation. In addition, grayscale intensity normalization was performed by centering and scaling the image intensities to a range of 0-255, with a fixed bin width of 25 for discretization, ensuring consistent gray-level distribution across different scans.

Model establishment

(1) Clinical model: Clinical variables showing statistically significant differences ($P<0.05$) in the univariate analysis were included as independent variables, with LVSI status as the dependent variable. A clinical prediction model was constructed based on multivariate logistic regression analysis.

(2) Radiomics model: First, inter-observer reliability of the extracted radiomic features was assessed by calculating the intraclass correlation coefficient (ICC) based on the annotations from the two physicians. Features with ICC >0.8 were retained, indicating good reproducibility. Subsequently, these retained features underwent standardization using Z-score normalization. Subsequently, least absolute shrinkage and selection operator (LASSO) regression with 10-fold cross-validation was applied for further dimensionality reduction, selecting features most strongly correlated with LVSI status. The optimal penalty coefficient λ (lambda. min) was determined through cross-validation, ultimately yielding a set of core features with nonzero coefficients. The radiomics score (Radscore) for each patient was calculated as a linear combination of these features. A ra-

diomics model was constructed with the Rad-score as the independent variable and LVSI status as the dependent variable.

(3) Combined model: significant predictors identified in the clinical model alongside the Rad-score were incorporated into a multivariate logistic regression analysis to construct the final combined predictive model.

Statistical analysis

All statistical analyses were performed using the United Imaging Research Platform software (version 2.0; United Imaging Intelligence, Shanghai, China) and SPSS (version 25.0; IBM Corp., Armonk, NY, USA). Continuous variables following a normal distribution were expressed as mean ± standard deviation and compared using the independent samples t-test, while non-normally distributed variables were presented as median (interquartile range, IQR) and compared using the Mann-Whitney U test. Categorical variables were described as frequencies (percentages) and analyzed with the Chi-squared test or Fisher's exact test, as appropriate.

Radiomics feature reproducibility was assessed using the ICC, and features with ICC >0.8 were retained. After Z-score standardization, LASSO regression with 10-fold cross-validation was applied to select the most predictive features and calculate the Rad-score.

Univariate logistic regression analysis was performed to screen clinical variables (entry criterion: P<0.10), followed by multivariable logistic regression with backward stepwise selection to establish the clinical model. The radiomics model was built using the Rad-score as the independent predictor. The combined model was constructed by integrating both clinical predictors and the Rad-score. Model discrimination was evaluated using the area under the receiver operating characteristic curve (AUC), with comparisons between models performed via DeLong's test. Calibration was assessed using calibration plots and the Hosmer-Lemeshow goodness-of-fit test. Clinical utility was quantified using decision curve analysis (DCA). All statistical tests were two-sided, and a *P* value <0.05 was considered statistically significant.

Results

Baseline characteristics of the training set and validation set

The training and validation cohorts included 244 and 58 patients, respectively (**Table 1**). There was no statistical difference in baseline demographic or clinical characteristics between the two groups, indicating good comparability.

Univariate analysis in the training set

In the training set, 92 cases were classified into the LVSI-positive group and 152 cases into the LVSI-negative group (**Table 2**). The average tumor diameter in the LVSI-positive group was significantly larger than that in the LVSI-negative group (51.25 ± 2.23 mm vs 50.06 ± 1.89 mm, P<0.001). In addition, the proportions of patients with poor differentiation (68.48% vs 44.74%, P<0.001), positive cEMVI (66.30% vs 48.03%, P=0.005), and CEA≥5 μg/L (63.04% vs 45.39%, P=0.001) were significantly higher in the LVSI-positive group than in the LVSI-negative group. No statistical differences were observed in other variables.

Construction of a clinical prediction model

Variables with statistical significance in the univariate analysis were included in the multivariate Logistics regression analysis to construct a clinical prediction model (**Table 3**). The model identified four independent predictors of LVSI: tumor diameter (OR=1.38, 95% CI: 1.18-1.61, P<0.001), degree of differentiation (OR=2.83, 95% CI: 1.57-5.09, P<0.001), cEMVI (OR=2.56, 95% CI: 1.41-4.63, P=0.002), and CEA level (OR=1.91, 95% CI: 1.07-3.40, P=0.028).

Screening of radiomic features

In this study, the radiomics features were preliminarily screened using the ICC test, and a total of 704 features with good reproducibility were retained. After 10-fold cross-validation and dimensionality reduction using LASSO regression, four radiomic features with non-zero coefficients were selected to construct the radiomics prediction model. The LASSO regression process is illustrated in **Figure 2A**, **2B**, and the four radiomic features are shown in **Figure 2C**.

Table 1. Patient characteristics in the training set and the validation set

Variables	Total (n=302)	Validation set (n=58)	Training set (n=244)	Statistic	*P*
Age, Mean ± SD	67.01 ± 9.10	67.34 ± 8.85	66.93 ± 9.18	t=0.31	0.753
Sex, n (%)				X^2=0.33	0.565
Female	115 (38.08)	24 (41.38)	91 (37.30)		
Male	187 (61.92)	34 (58.62)	153 (62.70)		
BMI, Mean ± SD	23.75 ± 3.52	23.53 ± 3.67	23.81 ± 3.49	t=-0.54	0.590
Tumor diameter, Mean ± SD (mm)	50.51 ± 2.07	50.39 ± 1.87	50.52 ± 2.11	t=-0.41	0.683
Tumor location, n (%)				χ^2=0.40	0.529
Left hemicolon	157 (51.99)	28 (48.28)	129 (52.87)		
Right hemicolon	145 (48.01)	30 (51.72)	115 (47.13)		
Differentiation degree, n (%)				χ^2=0.55	0.458
Moderately/highly differentiated	143 (47.35)	30 (51.72)	113 (46.31)		
Poorly differentiated	159 (52.65)	28 (48.28)	131 (53.69)		
cEMVI, n (%)				χ^2=0.19	0.661
Negative	138 (45.70)	28 (48.28)	110 (45.08)		
Positive	164 (54.30)	30 (51.72)	134 (54.92)		
Perirectal fat infiltration, n (%)				χ^2=0.52	0.470
Negative	133 (44.04)	28 (48.28)	105 (43.03)		
Positive	169 (55.96)	30 (51.72)	139 (56.97)		
CEA, n (%)				χ^2=0.08	0.779
<5 μg/L	146 (48.34)	29 (50.00)	117 (47.95)		
≥5 μg/L	156 (51.66)	29 (50.00)	127 (52.05)		
CA19-9, n (%)				χ^2=0.55	0.457
<37 U/mL	102 (33.77)	22 (37.93)	80 (32.79)		
≥37 U/mL	200 (66.23)	36 (62.07)	164 (67.21)		
Preoperative TNM stage				χ^2=0.22	0.637
Early stage (I-II)	226 (74.83)	42 (82.76)	184 (75.41)		
Advanced stage (III)	76 (25.17)	16 (27.59)	60 (24.59)		

Notes: BMI, body mass index; cEMVI, CT-detected extramural vascular invasion; CEA, carcinoembryonic antigen; CA19-9, carbohydrate antigen 19-9.

The ICC values for the four selected features were as follows: Shape_Maximum3DDiameter (ICC=0.92), GLCM_Correlation (ICC=0.87), GLRLM_LongRunEmphasis (ICC=0.89), and Wavelet_HHL_GLCM_Contrast (ICC=0.85), indicating excellent inter-observer reproducibility. Among these, the shape feature Maximum 3D Diameter reflected the overall tumor size, while GLCM_Correlation quantified local gray-level dependencies within the tumor texture. GLRLM_LongRunEmphasis characterized the presence of long, homogeneous gray-level runs, indicating intratumoral heterogeneity. Additionally, the wavelet-derived feature Wavelet_HHL_GLCM_Contrast captured fine-scale textural variations after frequency decomposition. Rad-score = 0.25* Shape_Maximum3DDiameter + 0.21* GLCM_Correlation + 0.09* GLRLM_LongRunEmphasis + 0.04* Wavelet_HHL_GLCM_Contrast.

Construction of the combined model

The combined prediction model integrating clinical features and radiomics features is shown in **Figure 3**. The model incorporated tumor diameter, degree of differentiation, cEMVI status, CEA level, and the Rad-score. The logistic regression equation of this model was as follows: Logit (P) = -28.6 + 0.37* tumor diameter + 1.26* degree of differentiation + 0.89* cEMVI + 0.80* CEA + 13.02* Rad-score.

Model performance analysis

In the training set, the combined model reached an AUC of 0.90 (95% CI: 0.86-0.94), significantly higher than that of the simple clinical model (Delong test, Z=-4.937, P<0.001) and the Rad-score model (DeLong test, Z=-3.426, P=0.001) (**Figure 4A**; **Table 4**). The combined

Table 2. Comparison of baseline characteristics between LVSI-positive and LVSI-negative patients in the training set

Variables	Total (n=244)	LVSI-negative group (n=152)	LVSI-positive group (n=92)	Statistic	*P*
Age, Mean ± SD	66.93 ± 9.18	67.20 ± 8.52	66.47 ± 10.19	t=0.61	0.544
Sex, n (%)				χ^2=0.13	0.720
Female	91 (37.30)	58 (38.16)	33 (35.87)		
Male	153 (62.70)	94 (61.84)	59 (64.13)		
BMI, Mean ± SD	23.81 ± 3.49	23.90 ± 3.53	23.64 ± 3.43	t=0.57	0.568
Tumor diameter, Mean ± SD (mm)	50.51 ± 2.11	50.06 ± 1.89	51.25 ± 2.23	t=-4.46	<0.001
Tumor location, n (%)				χ^2=2.83	0.092
Left hemicolon	129 (52.87)	74 (48.68)	55 (59.78)		
Right hemicolon	115 (47.13)	78 (51.32)	37 (40.22)		
Differentiation degree, n (%)				χ^2=12.99	<0.001
Moderately/highly differentiated	113 (46.31)	84 (55.26)	29 (31.52)		
Poorly differentiated	131 (53.69)	68 (44.74)	63 (68.48)		
cEMVI, n (%)				χ^2=7.73	0.005
Negative	110 (45.08)	79 (51.97)	31 (33.70)		
Positive	134 (54.92)	73 (48.03)	61 (66.30)		
Perirectal fat infiltration, n (%)				χ^2=0.41	0.520
Negative	105 (43.03)	63 (41.45)	42 (45.65)		
Positive	139 (56.97)	89 (58.55)	50 (54.35)		
CEA, n (%)				χ^2=7.15	0.007
<5 μg/L	117 (47.95)	83 (54.61)	34 (36.96)		
≥5 μg/L	127 (52.05)	69 (45.39)	58 (63.04)		
CA19-9, n (%)				χ^2=1.85	0.174
<37 U/mL	80 (32.79)	45 (29.61)	35 (38.04)		
≥37 U/mL	164 (67.21)	107 (70.39)	57 (61.96)		
Preoperative TNM stage				χ^2=2.72	0.099
Early stage (I-II)	184 (75.41)	120	64		
Advanced stage (III)	60 (24.59)	32	28 ()		

Notes: BMI, body mass index; cEMVI, CT-detected extramural vascular invasion; CEA, carcinoembryonic antigen; CA19-9, carbohydrate antigen 19-9.

Table 3. Construction of clinical prediction models

Variables	β	S.E	Z	*P*	OR (95% CI)
Differentiation degree					
Moderately/highly differentiated					1.00 (Reference)
Poorly differentiated	1.04	0.30	3.48	<0.001	2.83 (1.57-5.09)
cEMVI					
Negative					1.00 (Reference)
Positive	0.94	0.30	3.10	0.002	2.56 (1.41-4.63)
CEA					
<5 μg/L					1.00 (Reference)
≥5 μg/L	0.65	0.29	2.20	0.028	1.91 (1.07-3.40)
Tumor diameter	0.32	0.08	4.10	<0.001	1.38 (1.18-1.61)

Notes: cEMVI, CT-detected extramural vascular invasion; CEA, carcinoembryonic antigen.

model demonstrated an accuracy of 0.82, a sensitivity of 0.80, and a specificity of 0.86, indicating that it significantly reduced the misclassification rate while maintaining high sensi-

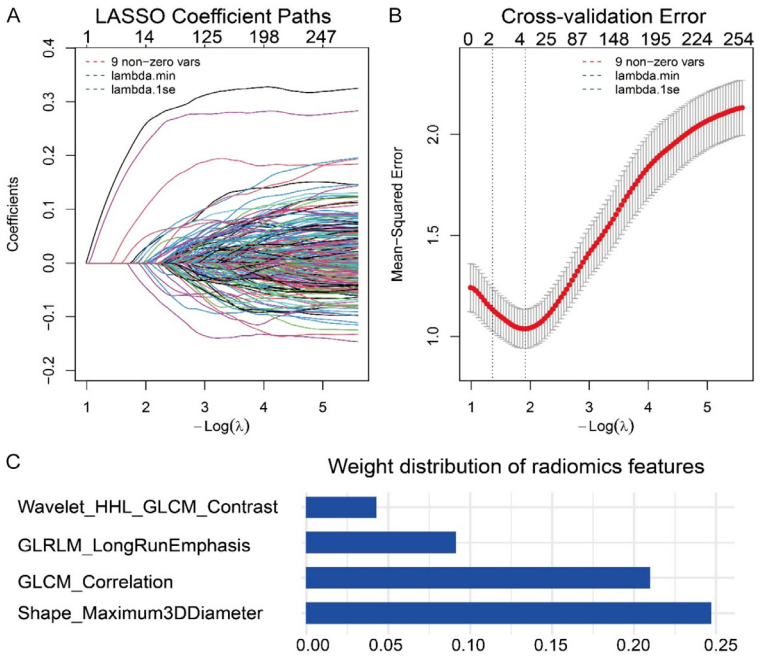

Figure 2. The process of radiomics feature screening. A. 10-fold cross-validation result; B. LASSO regression coefficient distribution map; C. Optimal radiomics features and their respective weights. Note: LASSO, least absolute shrinkage and selection operator.

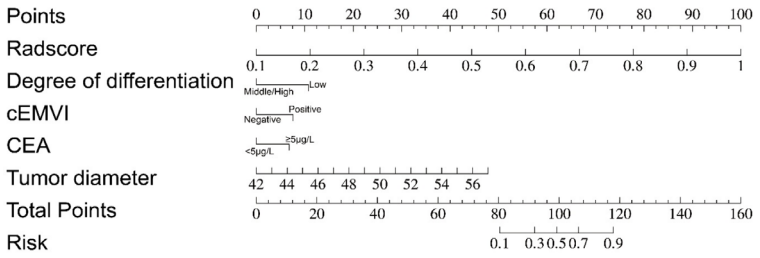

Figure 3. Joint prediction model based on the nomogram.

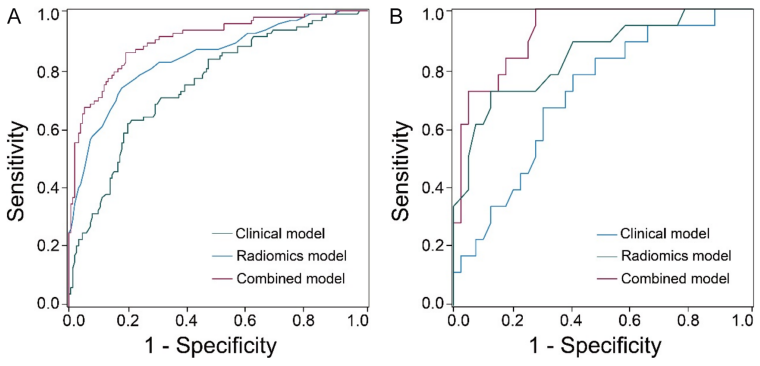

Figure 4. ROC curve analysis in the training set (A) and the validation set (B). Note: ROC, receiver operating characteristic.

tivity. In the validation set, the combined model still maintained excellent predictive performance, with an AUC of 0.92 (95% CI: 0.86-0.99), significantly superior to the clinical model (DeLong test, Z=-2.902, P=0.004) (**Figure 4B**; **Table 4**). The combined model also showed numerically higher performance compared with the Rad-score model. Although the statistical difference did not reach a significant level, the combined model performed the best in terms of accuracy (0.81) and specificity (1.00), further supporting its robustness and generalizability across different populations. Direct comparison between the training and validation cohorts revealed no significant difference in the predictive performance of the combined model (AUC: 0.90 vs 0.92, DeLong test, Z=-0.633, P=0.527), indicating stable predictive performance across different patient groups.

Model goodness-of-fit test

The goodness of fit of the model was evaluated using the calibration curve and the Hosmer-Lemeshow test. The results showed that in the training set, there was no significant difference between the predicted probabilities and the actual outcomes (x^2=10.20, Hosmer-Lemeshow P=0.252), indicating good model calibration (**Figure 5A**). In the validation set, the combined model also showed good agreement between predicted and observed outcomes (x^2=8.74, Hosmer-Lemeshow P=0.364) (**Figure 5B**).

Clinical utility of the model

DCA are shown in **Figure 6**. In the training set, when the threshold probability ranged from 0.1 to 0.9, the curve of the combined model consistently remained above the "treat-

Table 4. Analysis of model performance

Model	AUC	Accuracy	Sensitivity	Specificity	DeLong test	
					Z value	*P* value
Training set						
Clinical model	0.75 (0.69-0.81)	0.73	0.80	0.62	-4.937	<0.001
Radiomics model	0.84 (0.79-0.89)	0.79	0.82	0.74	-3.426	0.001
Combined model	0.90 (0.86-0.94)	0.82	0.80	0.86	Ref	Ref
Validation set						
Clinical model	0.71 (0.57-0.85)	0.66	0.60	0.78	-2.902	0.004
Radiomics model	0.84 (0.73-0.96)	0.83	0.88	0.72	-1.942	0.052
Combined model	0.92 (0.86-0.99)	0.81	0.72	1.00	Ref	Ref
Combined model (Training vs Validation)	0.90 vs 0.92	0.82 vs 0.81	0.80 vs 0.72	0.86 vs 1.00	-0.633	0.527

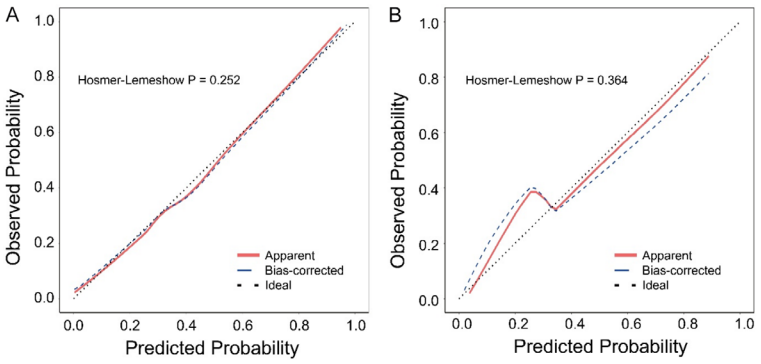

Figure 5. Calibration performance of the predictive model in the training set (A) and the validation set (B).

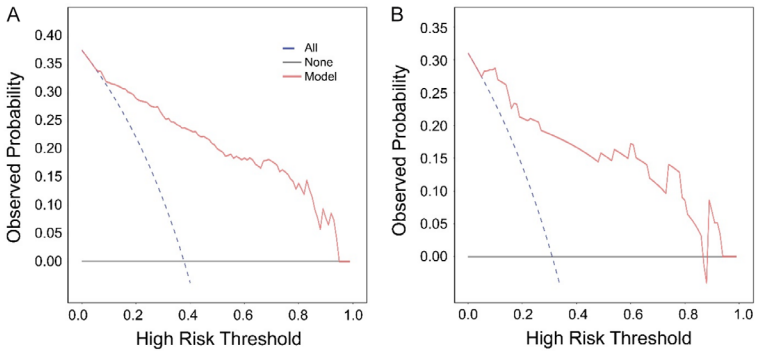

Figure 6. Clinical decision curve analysis in the training set (A) and the validation set (B).

all" strategy curve, suggesting that using the model to guide clinical decision-making within this threshold range could provide a sustained positive net benefits (**Figure 6A**). Specifically, the net benefit of the combined model exceeded that of the "treat-all" strategy by more than 0.10 when the risk threshold was between 0.25 and 0.78; the maximum net benefit difference (0.24) between the model and the "treat-all" strategy was achieved at a threshold probability of 0.38. Similarly, in the validation set, the curve of the combined model remained consistently higher than the "treat-all" strategy within the high-risk threshold range of 0.1 to 0.8, and was significantly superior to the "treat-non" strategy, further confirming the good clinical practicality of the model across different populations (**Figure 6B**). In the validation cohort, the net benefit advantage over the "treat-all" strategy remained above 0.10 across threshold probabilities of 0.20 to 0.60, peaking at a difference of 0.19 at a threshold probability of 0.33. These findings demonstrate that the combined model provides robust and clinically meaningful improvements in net benefit across a wide range of clinically relevant risk thresholds in both the training and validation cohorts.

Discussion

Colon cancer is one of the most prevalent malignant tumors of the digestive system worldwide, and its disease burden continues to increase in China [20]. LVSI is a significant pathological indicator in colorectal cancer, showing a close association with lymph node metastasis, distant metastasis, and poor prog-

nosis [21]. Chen et al. [22] reported that LVSI was significantly associated with lymphatic metastasis in colon cancer. However, LVSI diagnosis currently relies on postoperative pathological examination, limiting its application in guiding preoperative personalized treatment decision-making. This study successfully constructed and validated a combined model integrating clinical characteristics with CT radiomics for the non-invasive preoperative prediction of LVSI status in patients with colon cancer. The Results demonstrated that the combined model achieved outstanding discriminatory capability in both the training set (AUC= 0.90) and validation set (AUC=0.92), significantly outperforming either the clinical model or the radiomics model alone. Calibration curve and decision curve analyses further confirmed the good calibration and favorable clinical utility of the model. This study provides a robust tool for preoperative risk stratification in colorectal cancer patients, supporting its integration into existing clinical workflows. In current practice, decisions regarding adjuvant chemotherapy in stage II colon cancer and the extent of lymphadenectomy are largely based on postoperative pathological assessment LVSI, often leading to delayed or suboptimal individualized plans [7, 8]. The preoperative predictive model proposed in this study may help address this gap by identifying patients at high risk of LVSI before surgery, enabling clinicians to proactively adjust treatment strategies rather than relying on postoperative pathological confirmation.

The univariate analysis demonstrated that patients in the LVSI-positive group exhibited significantly higher mean tumor diameter, higher proportions of patients with poor differentiation and positive cEMVI, and elevated CEA levels compared to the LVSI-negative group. These findings further support the clinical relevance of the model, as the identified risk factors are routinely assessed during preoperative evaluation, facilitating seamless integration of the model into existing clinical decision-making system. Furthermore, multivariate logistic regression analysis confirmed that all these indicators were independent risk factors for LVSI. These findings are highly consistent with current understanding of colorectal cancer pathophysiology. Emile et al. [7] reported a strong correlation between LVSI and lymph node metastasis (LNM) as well as poorer overall survival. In the clinical prediction model developed by Niu et al. [23] based on 83,430 colon cancer patients, tumor indicators such as tumor diameter, grade, and stage were identified as independent predictors of LNM. From a biological perspective, an increase in tumor diameter may reflect enhanced tumor proliferation activity [24]. Tumor growth is not merely a simple increase in volume but rather an evolutionary process. During rapid proliferation, tumor cells tend to select subclones with greater invasiveness and proliferative capacity [25, 26]. These more aggressive subpopulations gradually become dominant, leading to an increased tendency to infiltrate surrounding tissues. Furthermore, previous research has suggested that when tumor diameter exceeds a certain threshold, the central region may develop hypoxia due to insufficient blood supply [27]. Hypoxia induces tumor cells to overexpress hypoxia-inducible factor-1α (HIF-1α), which subsequently activates multiple downstream pathways involved in angiogenesis (e.g., VEGF), cell invasion, and epithelial-mesenchymal transition (EMT), thereby creating favorable microenvironment for LVSI. Poorly differentiated tumor cells exhibit reduced cellular adhesion and increased proliferative activity, rendering them more prone to detaching from the primary site and invading vascular spaces [28]. In addition, cEMVI, as a key CT imaging indicator suggesting tumor invasion of blood vessels, is closely related to the pathological process of tumor cell invasion into vascular-interstitial space [29]. Elevated CEA levels reflect tumor burden and activity, and their potential co-regulation with angiogenesis-promoting factors may jointly create a tumor microenvironment conducive to vascular invasion [30, 31]. These clinical indicators collectively establish a framework for the clinical assessment of LVSI risk across multiple dimensions, including tumor burden, cellular malignancy, macroscopic morphology, and systemic tumor activity.

The advantage of radiomics lies in its ability to extract information about intratumoral heterogeneity that is imperceptible to the naked eye. In this study, four core features identified - Maximum 3D Diameter, GLCM_Correlation, GLRLM_LongRunEmphasis, and Wavelet_HHL_GLCM_Contrast - quantify tumor heterogeneity from distinct perspectives, showing potential associations with the biological mechanisms underlying LVSI. Among these, Maximum 3D

Diameter directly reflects tumor volume, which is closely correlated with increased proliferative activity and hypoxia in the tumor core [27, 32]. As tumors grow beyond a critical size, insufficient vascular supply induces overexpression of HIF-1α, subsequently upregulating genes involved in angiogenesis (e.g., VEGF) and EMT - key processes enabling tumor cells to invade lymphovascular spaces [25, 27]. This aligns with our clinical observation that tumor diameter serves as an independent risk factor for LVSI. GLCM_Correlation, which quantifies spatial gray-level uniformity, exhibits lower values in LVSI-positive tumors, indicating microstructural disorganization [33]. Such disorganization may stem from abnormal extracellular matrix (ECM) remodeling - tumor cells secrete matrix metalloproteinases (MMPs) to degrade collagen and fibronectin, disrupting tissue integrity and creating pathways for lymphovascular infiltration [17, 34]. Consequently, reduced GLCM_Correlation may indirectly reflect enhanced ECM degradation and invasive potential, core biological traits facilitating LVSI. GLRLM_LongRunEmphasis represents the presence of long runs of homogeneous gray-level pixels, and is often correlateed with intratumoral necrotic or fibrotic regions [35]. Necrosis-induced inflammation can trigger the release of cytokines (e.g., TNF-α, IL-6), which may promote vascular permeability and lymphangiogenesis. In addition, fibrotic regions may act as a "scaffold" for tumor cell migration. Therefore, elevated GLRLM_LongRunEmphasis values may indicate a tumor microenvironment conducive to LVSI, linking structural uniformity to pro-invasive biological signals. Wavelet_HHL_GLCM_Contrast, derived from high-frequency wavelet decomposition, captures fine-scale textural variations and reflects heterogeneity at the tumor-stroma interface [36]. This interface represents a critical site for crosstalk between tumor cells and stromal cells, including cancer-associated fibroblasts (CAFs). CAFs can secrete growth factors (e.g., TGF-β) that promote EMT in tumor cells, enhancing tumor cell motility and invasiveness to penetrate lymphovascular walls [37]. The association of this feature with LVSI may therefore reflect subtle interface alterations at the tumor-stroma boundary driven by tumor-microenvironment interactions. Collectively, these radiomic features may reflect key biological characteristics associated with LVSI: Maximum 3D Diameter and GLRLM_LongRunEmphasis primarily represent tumor burden and internal structural homogeneity/heterogeneity related to growth patterns; whereas GLCM_Correlation and Wavelet_HHL_GLCM_Contrast capture micro-architectural disorganization and local invasiveness at the tumor-stroma interface, both of which are hallmarks of aggressive tumor phenotypes and vascular invasion [38, 39]. These quantitative imaging parameters enable radiomics models to reveal deep-level tumor characteristics that extend beyond conventional radiological interpretation. The results of this study show that the combined model can achieve the best predictive performance, which may be attributed to the complementary nature of clinical features and radiomics features. Clinical features provide explicit biological information directly linked to disease mechanisms, whereas radiomics features offer highly-dimensional, quantitative, yet "black-box" data concerning the spatial heterogeneity within tumors [40]. For instance, even when two tumors present with similar size, differentiation grade, and CEA levels, their internal textural heterogeneity may differ substantially. Radiomics analysis is capable of capturing these subtle variations, which may reflect different risks of LVSI. Incorporating Rad-score into clinical models effectively integrates the tumor's macroscopic phenotype (clinical indicators) with microscopic textural features (imaging informatics), thereby enabling a more comprehensive and multidimensional assessment of its invasive potential. The statistically significant results of the DeLong test confirm that the enhancement in predictive performance achieved through integration is not coincidental.

For clinical application, the following adjustments are proposed based on model predictions: (1) For stage II colon cancer patients predicted to be LVSI-positive, adjuvant chemotherapy (e.g., 5-fluorouracil-based regimens) should be considered to reduce the risk of occult metastasis, aligning with ASCO guidelines [7]; (2) During surgical planning, a predicted high risk of LVSI may warrant extended lymphadenectomy (beyond standard D2 dissection) to ensure complete resection of potential micrometastatic nodes; (3) For locally advanced colon cancer, preoperative identification of LVSI risk could guide neoadjuvant therapy selection to downstage tumors and reduce

vascular invasion before surgery. These adjustments are feasible as the model is based on routine contrast-enhanced CT and clinical data, requiring no additional invasive procedures or cost.

This study has several limitations that should be acknowledged during clinical translation. First, as a single-center retrospective study, our validation was performed on a temporally independent but relatively small cohort (n=58) from the same institution. We have re-verified the validation set and confirmed the specificity of the combined model reached 1.00, with all LVSI-negative cases (28/28) correctly identified. However, this perfect specificity is likely overestimated due to the small sample size and limited number of LVSI-negative cases (n=28) in the validation set. Small cohorts are inherently prone to sampling bias and reduced statistical representativeness, failing to capture the full spectrum of clinical heterogeneity (e.g., rare tumor subtypes, complex comorbidities, or subtle variations in tumor biology) that exists in large, diverse patient populations. Additionally, the wide 95% CI of the specificity (0.87-1.00) further reflects the uncertainty of this estimate in real-world clinical practice. Thus, the model's specificity cannot be regarded as universally reproducible, and future larger-scale multicenter prospective studies with balanced LVSI-positive/negative distributions are required to validate its true performance and to avoid overoptimistic inferences. Second, the reproducibility of radiomics analysis faces challenges: variations in scanning parameters and reconstruction algorithms across different CT devices may affect feature stability, while the subjectivity of manually delineating tumor regions introduces bias. This necessitates future efforts to standardize image acquisition protocols and develop automated segmentation algorithms. Third, several practical issues must be addressed before its clinical translation, including the seamless integration of model outputs into clinical decision-making systems, the determination of optimal risk thresholds for intervention based on cost-benefit analysis, and the evaluation of the model's impact on clinical workflow efficiency. Crucially, the model should serve as a supportive tool rather than a substitute. A human-machine collaborative approach, combining model predictions with individualized patient circumstances, will remain essential for comprehensive assessment. Finally, current models offer insufficient explanation of underlying biological mechanisms. The precise relationship between imaging features and molecular processes such as lymphangiogenesis and EMT requires further elucidation through multi-omics integration analysis. These limitations indicate that while the model demonstrates promising predictive efficacy, its true clinical value remains contingent upon rigorous validation and systematic integration to overcome these challenges.

Conclusion

This study developed and validated a predictive model for LVSI in colon cancer by integrating clinical features and CT radiomics features. Tumor diameter, differentiation grade, cEMVI, and CEA were identified as independent risk factors for LVSI, while four core radiomic features effectively quantified tumor heterogeneity. The combined model exhibited excellent performance, with AUCs of 0.90 and 0.92 in the training and validation sets, respectively, outperforming the clinical and radiomics models alone. It also showed good calibration and meaningful clinical net benefits. This non-invasive model enables accurate preoperative LVSI prediction, aiding in individualized decisions on adjuvant chemotherapy and surgical scope.

Disclosure of conflict of interest

None.

Address correspondence to: Huajun Yu, Department of Radiology, Zhejiang Hospital, No. 12, Lingyin Road, Xihu District, Hangzhou 310013, Zhejiang, China. Tel: +86-0571-81595050; E-mail: yhjzjyy@163.com

References

[1] Audisio A, Fazio R, Daprà V, Assaf I, Hendlisz A and Sclafani F. Neoadjuvant chemotherapy for early-stage colon cancer. Cancer Treat Rev 2024; 123: 102676.

[2] Jiang D, Wu Y, Liu L, Shen Y, Li T, Lu Y, Wang P, Sun C, Wang K, Wang K and Ye H. Burden of gastrointestinal tumors in Asian countries, 1990-2021: an analysis for the global burden of disease study 2021. Clin Epidemiol 2024; 16: 587-601.

[3] Zhan Z, Chen B, Lin W, Chen X, Huang R, Yang C and Guo Z. Rising burden of colon and rec-

tum cancer in China: an analysis of trends, gender disparities, and projections to 2030. Ann Surg Oncol 2025; 32: 3361-3371.
[4] Aliseda D, Arredondo J, Sánchez-Justicia C, Alvarellos A, Rodríguez J, Matos I, Rotellar F, Baixauli J and Pastor C. Survival and safety after neoadjuvant chemotherapy or upfront surgery for locally advanced colon cancer: meta-analysis. Br J Surg 2024; 111: znae021.
[5] Özer L, Şenocak Taşçı E, Mutlu AU, Piyade B, Ramoğlu N, Ajredini M, Gürleyik D, Çeçen R, Dinçer SN, Musevitoğlu T, Göksel S, İnce Ü, Kayhan CK, Erdamar S, Yıldız İ and Aytaç E. Intramural component of venous, lymphatic, and perineural invasion in colon cancer: a threat or an illusion? Balkan Med J 2022; 39: 436-443.
[6] Cho SS, Park JW, Kang GH, Kim JH, Bae JM, Han SW, Kim TY, Kim MJ, Ryoo SB, Jeong SY and Park KJ. Prognostic impact of extramural lymphatic, vascular, and perineural invasion in stage II colon cancer: a comparison with intramural invasion. Dis Colon Rectum 2023; 66: 366-373.
[7] Vogel JD, Felder SI, Bhama AR, Hawkins AT, Langenfeld SJ, Shaffer VO, Thorsen AJ, Weiser MR, Chang GJ, Lightner AL, Feingold DL and Paquette IM. The American society of colon and rectal surgeons clinical practice guidelines for the management of colon cancer. Dis Colon Rectum 2022; 65: 148-177.
[8] Emile SH, Horesh N, Garoufalia Z, Wignakumar A, Boutros M and Wexner SD. Association between lymphovascular invasion and lymph node metastases in colon cancer: a national cancer database analysis. Colorectal Dis 2025; 27: e17256.
[9] Bompou E, Vassiou A, Baloyiannis I, Perivoliotis K, Fezoulidis I and Tzovaras G. Comparative evaluation of CT and MRI in the preoperative staging of colon cancer. Sci Rep 2024; 14: 17145.
[10] Miranda J, Torri GB, Andreia Maria da Silva M, Monjardim G, Mariussi M, Schmitt LG, Wiethan CP, Ghezzi TL, Ghezzi CLA, Altmayer S, Dias AB and Horvat N. CT diagnostic performance for preoperative staging of colon cancer: a systematic review and meta-analysis. Eur Radiol 2026; 36: 1506-1516.
[11] Wang R, Xu B, Sun M, Pang X, Wang X, Zhu J, Lian J and Lu H. Dynamic monitoring of serum CEA and CA19-9 predicts the prognosis of postoperative stage II colon cancer. Eur J Surg Oncol 2023; 49: 107138.
[12] Abbaspour E, Karimzadhagh S, Monsef A, Joukar F, Mansour-Ghanaei F and Hassanipour S. Application of radiomics for preoperative prediction of lymph node metastasis in colorectal cancer: a systematic review and meta-analysis. Int J Surg 2024; 110: 3795-3813.
[13] Warkentin MT, Al-Sawaihey H, Lam S, Liu G, Diergaarde B, Yuan JM, Wilson DO, Atkar-Khattra S, Grant B, Brhane Y, Khodayari-Moez E, Murison KR, Tammemagi MC, Campbell KR and Hung RJ. Radiomics analysis to predict pulmonary nodule malignancy using machine learning approaches. Thorax 2024; 79: 307-315.
[14] Qi YJ, Su GH, You C, Zhang X, Xiao Y, Jiang YZ and Shao ZM. Radiomics in breast cancer: current advances and future directions. Cell Rep Med 2024; 5: 101719.
[15] Huang Y, He L, Li Z, Chen X, Han C, Zhao K, Zhang Y, Qu J, Mao Y, Liang C and Liu Z. Coupling radiomics analysis of CT image with diversification of tumor ecosystem: a new insight to overall survival in stage I-III colorectal cancer. Chin J Cancer Res 2022; 34: 40-52.
[16] Abbaspour E, Karimzadhagh S, Monsef A, Joukar F, Mansour-Ghanaei F and Hassanipour S. Application of radiomics for preoperative prediction of lymph node metastasis in colorectal cancer: a systematic review and meta-analysis. Int J Surg 2024; 110: 3795-3813.
[17] Yang Y, Wei H, Fu F, Wei W, Wu Y, Bai Y, Li Q and Wang M. Preoperative prediction of lymphovascular invasion of colorectal cancer by radiomics based on 18F-FDG PET-CT and clinical factors. Front Radiol 2023; 3: 1212382.
[18] Peduzzi P, Concato J, Kemper E, Holford TR and Feinstein AR. A simulation study of the number of events per variable in logistic regression analysis. J Clin Epidemiol 1996; 49: 1373-9.
[19] Nagtegaal ID, Odze RD, Klimstra D, Paradis V, Rugge M, Schirmacher P, Washington KM, Carneiro F and Cree IA; WHO Classification of Tumours Editorial Board. The 2019 WHO classification of tumours of the digestive system. Histopathology 2020; 76: 182-188.
[20] Ilic M and Ilic I. Cancer of colon, rectum and anus: the rising burden of disease worldwide from 1990 to 2019. J Public Health (Oxf) 2024; 46: 20-29.
[21] Zwager LW, Bastiaansen BAJ, Montazeri NSM, Hompes R, Barresi V, Ichimasa K, Kawachi H, Machado I, Masaki T, Sheng W, Tanaka S, Togashi K, Yasue C, Fockens P, Moons LMG and Dekker E. Deep submucosal invasion is not an independent risk factor for lymph node metastasis in T1 colorectal cancer: a meta-analysis. Gastroenterology 2022; 163: 174-189.
[22] Long C, Cheng J, Feng M, Yan B, Li Y, Jiang W, Chen D and Yan J. Association of the tumor microenvironment collagen score and immunoscore with colon cancer lymph node metastasis. BMC Cancer 2025; 25: 506.
[23] Niu X and Cao J. Predicting lymph node metastasis in colorectal cancer patients: develop-

ment and validation of a column chart model. Updates Surg 2024; 76: 1301-1310.
[24] Ning FL, Gu WJ, Dai LZ, Du WY, Zeng YJ, Zhang JK, Abe M, Liu YL, Zhang R and Zhang CD. Identification and initial validation of maximal tumor area as a novel prognostic factor for overall and disease-free survival in patients with resectable colon cancer: a retrospective study. Int J Surg 2023; 109: 3407-3416.
[25] Feng H, Lyu Z, Zheng J, Zheng C, Wu Q, Liang W and Li Y. Association of tumor size with prognosis in colon cancer: a Surveillance, Epidemiology, and End Results (SEER) database analysis. Surgery 2021; 169: 1116-1123.
[26] Vogel JD, Felder SI, Bhama AR, Hawkins AT, Langenfeld SJ, Shaffer VO, Thorsen AJ, Weiser MR, Chang GJ, Lightner AL, Feingold DL and Paquette IM. The American society of colon and rectal surgeons clinical practice guidelines for the management of colon cancer. Dis Colon Rectum 2022; 65: 148-177.
[27] Bhattacharya R, Brown JS, Gatenby RA and Ibrahim-Hashim A. A gene for all seasons: the evolutionary consequences of HIF-1 in carcinogenesis, tumor growth and metastasis. Semin Cancer Biol 2024; 102-103: 17-24.
[28] Strous MTA, van der Linden RLA, Gubbels ALHM, Faes TKE, Bosscha K, Bronkhorst CM, Janssen-Heijnen MLG, de Bruïne AP and Vogelaar FJ. Node-negative colon cancer: histological, molecular, and stromal features predicting disease recurrence. Mol Med 2023; 29: 77.
[29] Guimarães RB, Pacheco EO, Ueda SN, Tiferes DA, Mazzucato FL, Talans A, Torres US and D'Ippolito G. Evaluation of colon cancer prognostic factors by CT and MRI: an up-to-date review. Abdom Radiol (NY) 2024; 49: 4003-4015.
[30] Samaille T, Falcoz A, Cohen R, Laurent-Puig P, André T, Taieb J, Auclin E and Vernerey D. A novel risk classification model integrating CEA, ctDNA, and pTN stage for stage 3 colon cancer: a post hoc analysis of the IDEA-France trial. Oncologist 2024; 29: e1492-e1500.
[31] Wang R, Xu B, Sun M, Pang X, Wang X, Zhu J, Lian J and Lu H. Dynamic monitoring of serum CEA and CA19-9 predicts the prognosis of postoperative stage II colon cancer. Eur J Surg Oncol 2023; 49: 107138.
[32] Li M, Xu G, Chen Q, Xue T, Peng H, Wang Y, Shi H, Duan S and Feng F. Computed tomography-based radiomics nomogram for the preoperative prediction of tumor deposits and clinical outcomes in colon cancer: a multicenter study. Acad Radiol 2023; 30: 1572-1583.
[33] Dai W, Mo S, Han L, Xiang W, Li M, Wang R, Tong T and Cai G. Prognostic and predictive value of radiomics signatures in stage I-III colon cancer. Clin Transl Med 2020; 10: 288-293.
[34] Abbaspour E, Karimzadhagh S, Monsef A, Joukar F, Mansour-Ghanaei F and Hassanipour S. Application of radiomics for preoperative prediction of lymph node metastasis in colorectal cancer: a systematic review and meta-analysis. Int J Surg 2024; 110: 3795-3813.
[35] Guo T, Cheng B, Li Y, Li Y, Chen S, Lian G, Li J, Gao M, Huang K and Huang Y. A radiomics model for predicting perineural invasion in stage II-III colon cancer based on computer tomography. BMC Cancer 2024; 24: 1226.
[36] Caruso D, Polici M, Zerunian M, Del Gaudio A, Parri E, Giallorenzi MA, De Santis D, Tarantino G, Tarallo M, Dentice di Accadia FM, Iannicelli E, Garbarino GM, Canali G, Mercantini P, Fiori E and Laghi A. Radiomic cancer hallmarks to identify high-risk patients in non-metastatic colon cancer. Cancers (Basel) 2022; 14: 3438.
[37] Chen ZY, Liu HZ, Shang ZJ, Luo GF and Zhang XZ. Nanomedicine for targeting cancer-associated fibroblasts in cancer therapy. Theranostics 2026; 16: 1545-1576.
[38] Aerts HJ, Velazquez ER, Leijenaar RT, Parmar C, Grossmann P, Carvalho S, Bussink J, Monshouwer R, Haibe-Kains B, Rietveld D, Hoebers F, Rietbergen MM, Leemans CR, Dekker A, Quackenbush J, Gillies RJ and Lambin P. Decoding tumour phenotype by noninvasive imaging using a quantitative radiomics approach. Nat Commun 2014; 5: 4006.
[39] Hong EK, Bodalal Z, Landolfi F, Bogveradze N, Bos P, Park SJ, Lee JM and Beets-Tan R. Identifying high-risk colon cancer on CT an a radiomics signature improve radiologist's performance for T staging? Abdom Radiol (NY) 2022; 47: 2739-2746.
[40] Jia J, Wang J, Zhang Y, Bai G, Han L and Niu Y. Deep learning and radiomic signatures associated with tumor immune heterogeneity predict microvascular invasion in colon cancer. Acad Radiol 2025; 32: 5267-5277.